

First muon acceleration and muon linear accelerator for measuring the muon anomalous magnetic moment and electric dipole moment

Masashi Otani

High Energy Accelerator Research Organization (KEK), Ibaraki 319-1106, Japan

**E-mail: masashio@post.kek.jp*

.....
Muon acceleration using a radio-frequency accelerator was recently demonstrated for the first time. Measurement of the muon anomalous magnetic moment and electric dipole moment at Japan Proton Accelerator Research Complex is the first experiment using accelerated muon beams, and construction will begin soon. The radio-frequency accelerator used in the experiment and the first muon acceleration are described in this paper.
.....

Subject Index C07, C31, G07

1. Introduction

A remarkable development of accelerator science from the beginning of the 20th century to the present has enabled the use of various quantum beams, such as electron, proton, and ion beams, and has opened the way to greater human understanding, including the discovery of the Higgs boson and quantum beam therapy etc. The acceleration of muons using a radio-frequency accelerator was recently demonstrated for the first time [1], and has opened a new era of accelerator science using accelerated muon beams.

A muon is an elementary particle similar to an electron, with an electric charge of $-e$ and a spin of $\frac{1}{2}$, but with a mass 200-times heavier. After the successful generation of muons using a proton driver half a century after their discovery during the study of cosmic-rays [2, 3], muons are now widely used in various scientific fields. In recent years, the demand for muon acceleration has been increasing in many different areas. For example, a muon collider, where muons are accelerated to a high energy for colliding, is one of the future plans of particle physics [4, 5]. In the material and life sciences, one promising application of muon acceleration is in the construction of a transmission muon microscope [6]. If the muons can be cooled to thermal temperature and subsequently re-accelerated, transmission muon microscopes will be realized. Among the future programs, a new experiment (E34 experiment) in the Materials and Life Science Experimental Facility (MLF) of the Japan Proton Accelerator Research Complex (J-PARC) is planning to measure the muon anomalous magnetic moment (a_μ) and search for the electric dipole moment (EDM) as a pioneer in muon acceleration [7].

Although the discovery of the Higgs boson using the Large Hadron Collider (LHC) has established the Standard Model (SM) as a successful description of particle interactions, we are still confronted with many problems that can be solved only through experimental clues.

One of the most interesting clues is the precise measurement of a_μ , which has paved the way for understanding the nature of elementary particles through the quantum effects. In a series of three experiments at European Organization for Nuclear Research (CERN) [8–10] and an experiment at Brookhaven National Laboratory (BNL) [11], successive improvements in the accuracy of the measurements had enabled a deeper understanding of the SM and there is a large discrepancy between measurements and predictions of the SM. After many years of scrutiny, challenging calculations and corrections were conducted by stimulated theorists and still 3.7 sigma deviation remains [12]. This discrepancy should be addressed by new measurements. A new experiment at Fermi National Accelerator Laboratory (FNAL E989 [13]) is currently being conducted, with the storage ring from the BNL experiment being reused. They published their first result in early FY2021 [14]. The result is consistent to that of the previous BNL experiment and the the tension between experiment and the SM calculation becomes 4.2 sigma. It strengthens the importance for confirming the tension with with independent measurements different from BNL and FNAL.

As described above, continuous studies have continued improving the accuracy of a_μ . In particular, the improvement of the beam has been one of the driving forces moving the measurements forward. Our ancestors at CERN, BNL, and FNAL have been struggling with beam-related uncertainties in their measurements because they use muons obtained directly from a pion decay with a large emittance. The J-PARC E34 experiment [7] aims to measure a_μ with a precision of 0.1 ppm using an unprecedentedly low-emittance muon beam realized by the acceleration of thermal muons.

The remainder of this paper is organized as follows. In Section 2, the J-PARC E34 experiment, particularly the radio-frequency linear accelerator (linac) dedicated to muons is described. Section 3 describes the first demonstration of muon acceleration. A summary and outlook are shown in Section 4.

2. Muon linac for the J-PARC E34 experiment

In this section, details of the muon linac will be described after successive descriptions explaining an overview of the J-PARC E34 experiment.

The J-PARC E34 experiment aims to measure a_μ with a precision of 0.1 ppm and search for the EDM with a sensitivity of approximately 10^{-21} e·cm using a low-emittance muon beam realized by an accelerated thermal muon beam. The total emittance in the transverse direction is required to be 1.5π mm mrad to realize the measurement with a 3 T compact MRI-type magnet with sufficient injection efficiency. The cyclotron radius with this magnet is 333 mm that is about a factor of 20 smaller than that for the BNL and FNAL experiments. Because of the high uniformity of the magnetic field in the muon storage region, the uncertainty due to the field uniformity is much smaller than in the BNL and FNAL experiments. Figure 1 shows the experimental setup. The pulsed high-power primary proton beam generates secondary surface muons produced by π^+ decay near the surface of the production target [16]. The produced surface muons are extracted and thermalized to form muoniums (bound state made up of a positive muon and an electron), which are then emitted into vacuum region adjacent to the muonium production target [17–19]. The paired electron in the muonium is knocked out by a laser, and thermal muon (3 keV/c) is generated. After acceleration to 300 MeV/c, the muon beam has an extremely low emittance such that it can be injected and stored in a high precision compact storage magnet [20, 21], where the time

dependence of the positrons from the muon decay is measured for the measurement of the anomalous spin precession [22, 23].

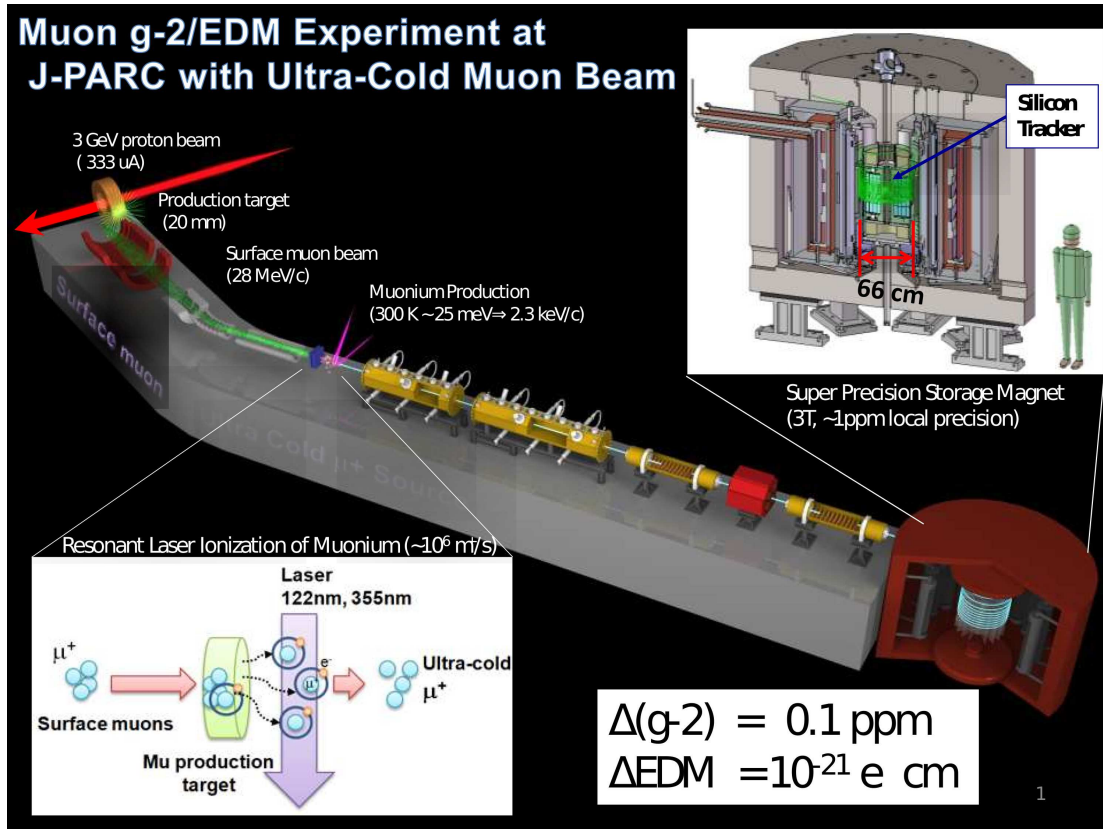


Fig. 1 Overview of the J-PARC E34 experiment.

2.1. Overview of muon linac

Because muons have a finite lifetime of approximately $2.2 \mu\text{s}$, they need to be accelerated faster to avoid decay losses to obtain the necessary experimental statistics. From this perspective, a linac is one of the best options for muon acceleration.

Owing to its intermediate mass between that of protons and electrons, the change in velocity upon acceleration is slower than that of electrons, as shown in Fig. 2. For this reason, both proton and electron linac technologies will be used to accelerate the muon to near the speed of light.

Accelerators should be designed appropriately to reduce costs. To reduce the expenses, a spare radio-frequency quadrupole (RFQ) of the J-PARC linac [24] will be used as a first stage acceleration. It operates with a resonant frequency of 324 MHz. The L-band high-power klystron developed for the KEKB linac upgrade [25] will be used as the RF power supply for the acceleration cavity in the high-energy section to achieve a further cost reduction.

A schematic of the muon linac is shown in Fig. 3. The RFQ bunches and accelerates the muons to 0.3 MeV after the initial electrostatic acceleration [26]. After the RFQ, an interdigital H-mode drift tube linac (IH-DTL) is employed during the particle velocity $\beta = 0.08$ to 0.28 (4 MeV) [27]. After the muon is accelerated to $\beta = 0.28$, a disk-and-washer (DAW)

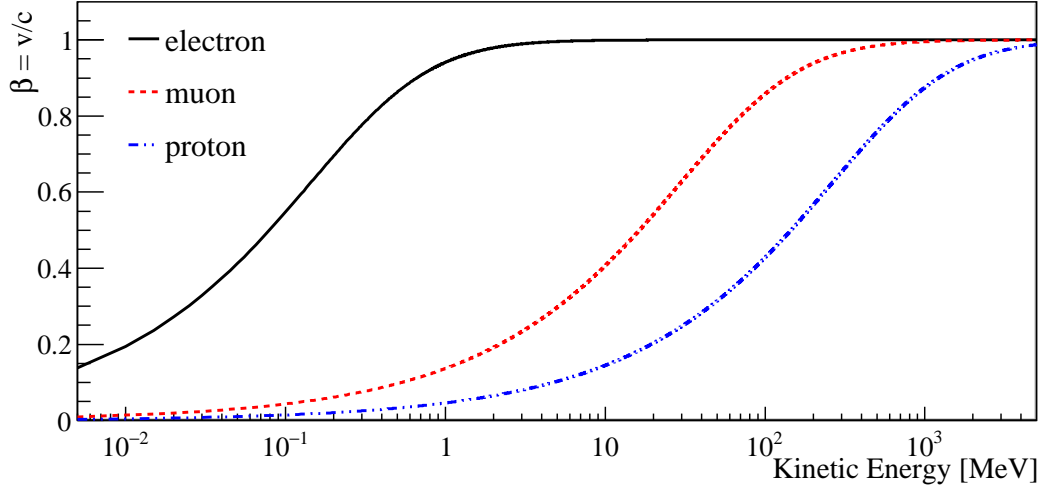


Fig. 2 Particle velocity as a function of kinetic energy for electron (black line), muon (red hatched line), and proton (blue dot-dash line)

type coupled cavity linac (CCL) with an operational frequency of 1296 MHz is employed [28]. Because the β variation is modest in the high- β region, to realize a sufficiently short distance, the design emphasis has been shifted to achieving a high accelerating gradient. A disk-loaded structure (DLS) traveling-wave linac is used when β is greater than 0.7 (42 MeV) [29]. The

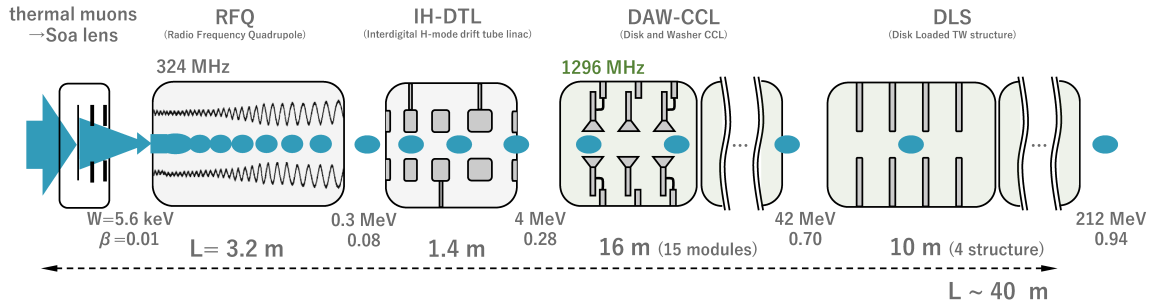


Fig. 3 Configuration of the muon linac. In this figure, W is kinetic energy and β is the ratio of the muon velocity to the speed of light.

2.2. Initial electrostatic acceleration

In front of the RFQ, there is an electrostatic lens called a Soa lens [30], which accelerates and extracts the thermal muons.

Figure 4 shows a schematic view of the Soa lens. The Soa lens consists of two mesh electrodes and three cylindrical electrodes. The first mesh electrode (target mesh) covers the downstream surface of the silica aerogel target. The laser ionization region is between the target mesh and second mesh electrode (S1). The voltage applied to the target mesh and S1 is set to 5.7 and 5.6 keV, respectively, corresponding to the input energy of the RFQ. The

dimensions of the electrodes are designed to cover the primary surface muons (rms size of 31 mm and 14 mm in the horizontal and vertical directions, respectively [31]) and to provide a sufficient extraction efficiency for ultra slow muons. The voltage applied to other electrodes (S2, S3 and S4) is determined using the simulation described below such that the phase space of the beam matched with the design acceptance of the RFQ and a high transmission efficiency is obtained.

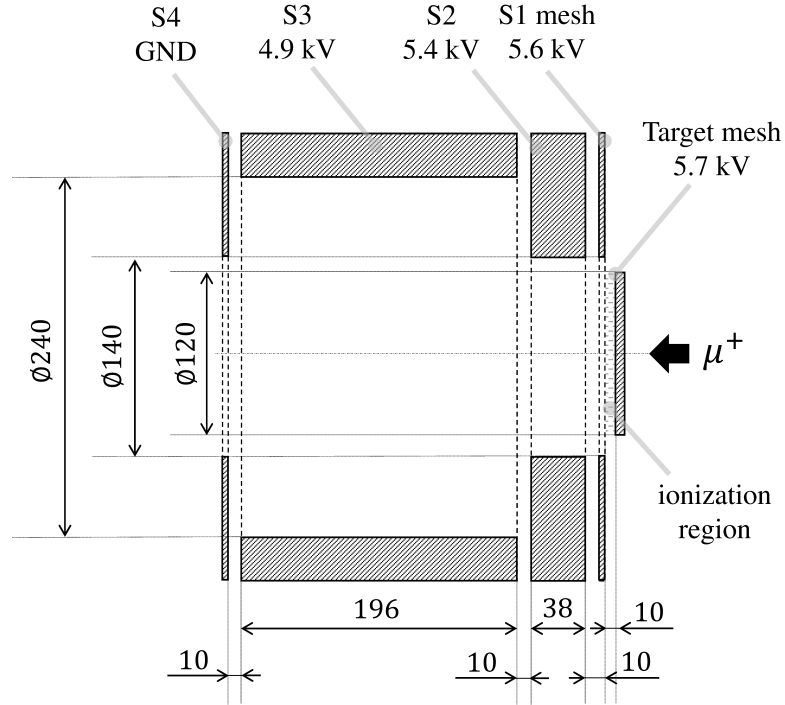


Fig. 4 Schematic of the SOA lens. Lengths in the figure are expressed in millimeters.

Input muon distributions are estimated using a simulation based on measurements. The simulation for a surface muon beamline (MLF H-line) is constructed using the g4beamline [16, 32]. The absolute number of surface muons is normalized by measurements from another beamline (MLF D-line [33]) that uses the same muon production target in J-PARC MLF. The stopping distribution inside the silica aerogel is estimated using GEANT4 [34]. The simulation for muonium diffusion is developed based on a three-dimensional random walk. The simulation parameters of the thermal temperature and the diffusion constant were determined from our measurements at Canada’s particle accelerator centre (TRIUMF) [18]. The muon trajectories are simulated using the GEANT4 simulation where the electrostatic field of the Soa lens calculated OPERA [35] is implemented.

Figure 5 shows the transverse phase space distributions at the entrance of the RFQ. The difference between the horizontal and vertical directions is due to the difference in the primary surface muon distribution at the entrance of the silica aerogel. Owing to the spatial distribution of the muoniums in the laser ionization region, the muons are distributed over time with a full width of approximately 10 ns. The transmission efficiency in the Soa lens is estimated to be 72%, including a 17% decay loss. Because the structure of the mesh

electrodes (target mesh and S1) is not implemented in the GEANT4 simulation, the transmission efficiency of the mesh electrode was estimated to be 78% based on the products of the aperture ratio of the two meshes. In total, the efficiency is 56% in the initial electrostatic acceleration.

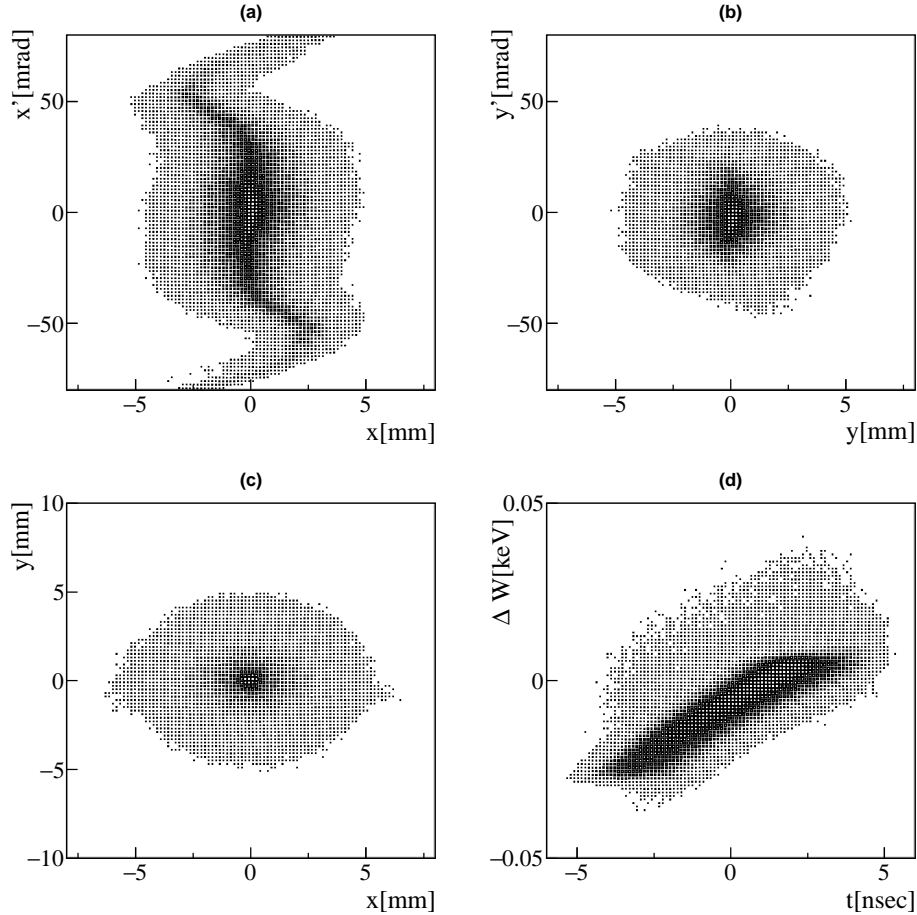


Fig. 5 Phase space distributions at the entrance of the RFQ: (a) Horizontal divergence angle x' vs. x , (b) the vertical divergence angle y' vs. y , (c) y vs. x , and (d) ΔW vs. time

2.3. RFQ

After the initial acceleration by the Soa lens, the RFQ accelerates the muons to 340 keV. In addition to the acceleration, the RFQ bunches the muons at a frequency of 324 MHz.

The principles of the RFQ were first invented in 1969 [37, 38] and they proved at Los Alamos National Laboratory (LANL) in 1980 [39]. The RFQ consists of a four electrodes excited with quadrupole-mode. The electrode is modulated longitudinally, generating the axial electric field. By changing modulation pattern gradually so that the synchronous phase is changed from -90 degree to higher, the beam bunching accomplished. Because the RFQ supply velocity-independent electric focusing, it has great advantage in a low-velocity part compared with conventional linacs that used velocity-dependent magnetic focusing.

Table 1 lists the design parameters of the RFQ for the muon acceleration along with that for negative hydrogen ion (H^-). To accelerate muons using the spare of the J-PARC RFQ, which was originally developed for H^- acceleration, the intervane voltage must be reduced to the mass ratio to match the particle velocity. As a result, the required power is reduced to the square of the mass ratio. The input and output energies are also scaled to the design velocity; the input and output β are 0.01 and 0.08, respectively.

Table 1 Parameters of the RFQ II for the H^- and muon acceleration.

	H^-	muon
Frequency (MHz)	324	
Number of cells	295	
Length (m)	3.17	
Intervane voltage (kV)	82.9	9.3
Power (kW)	330	4.2
Injection energy (keV)	50	5.6
Extraction energy (MeV)	3	0.34

In order to confirm that the RFQ can accelerate muons without any problems, particle simulations were performed using PARMTEQM [36]. Figure 6 shows the phase space distributions at the RFQ exit, and Table 2 summarizes the input and output beam parameters. The horizontal and vertical normalized rms emittances at the RFQ exit are 0.30 and 0.17 π mm mrad, respectively. The simulated transmission is 94.7%. Since the transit time through one cell of the RFQ is half the resonant frequency, the transit time through the entire RFQ can be calculated as $\frac{1}{324 \times 10^6} \times \frac{1}{2} \times 295 = 455$ ns. Ignoring relativistic corrections, the muon lifetime is 2.2 μ s, and the survival rate of muons passing through the RFQ is $\exp(-0.455/2.2) = 0.813$. Therefore, the total transmission is 77.0%.

The operation test of the RFQ has already been conducted [40]. The RFQ was powered on by a solid state amplifier at up to 6 kW and a 25 Hz repetition. Vacuuming is done with an ion pump and reaches 10^{-6} Pa. Figure 7 shows the forward, reflection, and pick-up power in the RFQ when 5 kW power is applied. There is a small reflection because the coupling was tuned to be overcoupled originally for a high current H^- beam. A few hours of operation at 5 kW was successfully achieved without any problems, such as an RF failure from a spark. The background associated with the RF operation was measured using a micro-channel plate detector connected downstream of the RFQ. The detector count rates were consistent and negligibly small with and without the RF operation, within a statistical uncertainty range of 0.1 Hz.

In conclusion, we are ready for a muon acceleration using the RFQ.

2.4. IH-DTL

After the initial acceleration and bunching by the RFQ, the IH-DTL accelerates the muons to 4.3 MeV.

The IH-DTL has alternating drift tubes up and down through the stem allowing the TE11 mode to be used for acceleration. The IH-DTL was first proposed in Japan in 1949 [41]. Although there were several efforts for this inventions [42–44], an IH-DTL was realized after

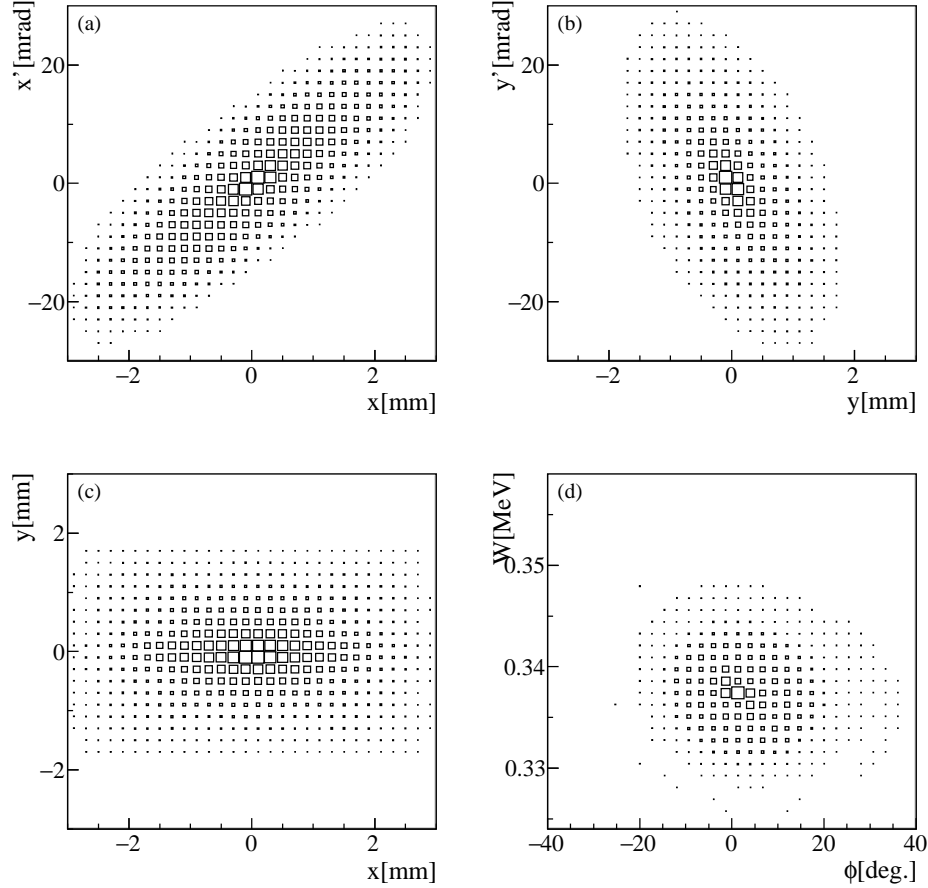


Fig. 6 Phase space distributions at the RFQ exit: (a) Horizontal divergence angle x' vs. x , (b) vertical divergence angle y' vs. y , (c) y vs. x , and (d) ΔW vs. rf phase (= time)

a quarter century as the heavy ion post-accelerator at the Munich tandem accelerator [45]. Compared to the conventional Arvarez DTL, a higher acceleration efficiency is achieved, particularly within the range of $\beta = 0.1$ – 0.2 [46]. In recent IH-DTLs, the alternating phase focusing (APF) method [47, 48], which was successfully implemented in the Hadron therapy machine [49], enables simultaneous focusing in the horizontal and vertical directions using only electric fields, resulting in a higher acceleration efficiency. Owing to the small focusing strength in the APF method, there is a limit to its use in high current machines, but it can be applied in the muon linac, which has a small current.

The IH-DTL with the APF method for accelerating muons was designed using several types of simulation software [27]. The arrangement of the drift tubes and acceleration gaps, i.e., the so-called longitudinal beam dynamics design, should be determined according to the evolution of the beam velocity, which is determined by the energy gain at each gap. Unlike conventional accelerating cavities where transverse focusing is performed conducted using additional elements such as quadrupoles, an APF cavity requires simultaneous non-independent longitudinal and transverse beam dynamics designs. This beam dynamics design was performed based on `linacsapf` [50], where the beam dynamics is calculated using the

Table 2 Input and output beam parameters of the beam dynamics simulation of the RFQ. In this table, α and β are Twiss parameters.

	Input	Output
α_x	0.32	-1.51
β_x [mm/mrad]	0.041	0.21
ε_x [π mm mrad, rms, normalized]	0.376	0.297
α_y	0.092	0.606
β_y [mm/mrad]	0.080	0.076
ε_y [π mm mrad, rms, normalized]	0.106	0.167
α_z	-	0.17
β_z [deg/MeV]	-	1360
ε_z [π MeV deg, rms, normalized]	-	0.0381
Time width	10 ns (full width)	-
Energy spread	0.00989 keV (rms)	-
Transmission		94.7%
Transient time		455 ns
Survival rate		81.3%
Transmission total		77.0%



Fig. 7 Forward, reflection wave, and pick-up power in RFQ with nominal power of 5 kW

so-called *drift-kick-drift* approximation. To achieve less emittance growth and a better transmission, a nonlinear optimization is applied to the synchronous phase array. The cavity was designed using CST-MW Studio [51] based on the beam dynamics design. In order to mitigate the peak electric field and obtain a higher efficiency, the dimensions of the drift tube were changed from [27]. Table 3 summarizes the basic parameters of the IH-DTL cavity.

The input distribution was given from the upstream RFQ simulation. The input was used for the beam dynamics simulation after simulation of the beam transport line to match the

Table 3 Parameters of the IH-DTL cavity. Because the frequency is tuned to 324 MHz with conductive tuners, the frequency shown here is slightly smaller than 324 MHz. In this table, $E_{surf.}$ is the surface electric field and E_{kp} is the Kilpatrick limit at 324 MHz (17.8 MV/m).

Parameters	Values
Frequency (MHz)	323.3
Number of cells	16
Length (m)	1.32
Synchronous phase [deg.]	-44+48
Unloaded Q	1.04×10^4
Power (kW)	322
Peak $E_{surf.}$ (MV/m)	35.3 ($\sim 1.99E_{kp}$)

beam to the IH-DTL. The beam dynamics simulation is performed using GPT [53]. Figure 8 shows the phase space distributions at the IH-DTL exit, and Table 4 summarizes the output beam parameters. The vertical emittance growth is larger than the horizontal one, which is due to the vertical meandering track caused by the vertical electric field and horizontal magnetic fields of the first and last cells, which is inevitable in IH-DTL structures. The transmission is 99.97% and it is sufficiently large. The beam transit time $t_{trans.}$ is 25 ns and the muon survival rate is calculated to be $\exp(t_{trans.}/\tau_\mu\bar{\gamma}) = 98.9\%$, where the average Lorentz factor during acceleration is labeled $\bar{\gamma}$ and τ_μ is the muon lifetime (2.2 μ s).

Table 4 Output beam parameters of the IH-DTL. In this table, α and β are Twiss parameters.

	Output
α_x	-4.3
β_x [mm/mrad]	0.38
ε_x [π mm mrad, rms, normalized]	0.316
α_y	-3.4
β_y [mm/mrad]	0.33
ε_y [π mm mrad, rms, normalized]	0.190
α_z	-1.0
β_z [deg/MeV]	174
ε_z [π MeV deg, rms, normalized]	0.0274
Transmission	99.97%
Transient time	25 ns
Survival rate	98.9%
Transmission total	98.9%

An error study of the beam dynamics was conducted by assuming several possible cases [52]. The error in the on-axis electric field owing to a fabrication error is estimated to be approximately 2% using the CST-MW Studio assuming a general fabrication error of

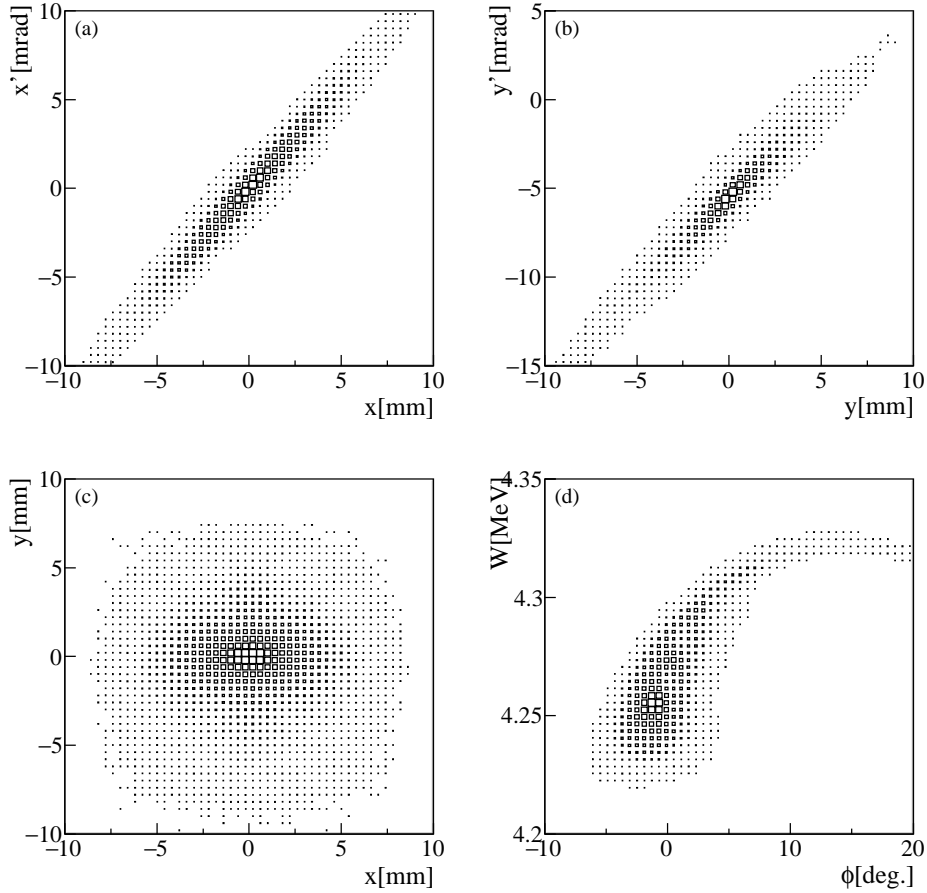


Fig. 8 Phase space distributions at the IH-DTL exit: (a) Horizontal divergence angle x' vs. x , (b) vertical divergence angle y' vs. y , (c) y vs. x , and (d) ΔW vs. rf phase (= time)

100 μm . The emittance growth due to the fabrication errors is estimated to be 10%, which still satisfies the requirement. It also shows that the error field can be controlled by some movable conductive tuners installed on the cavity side wall.

A prototype of the IH-DTL was fabricated (Fig. 9) to confirm the design and evaluate the performance [54]. The prototype was a three-piece design with two semi-cylindrical shells attached to the center frame where the drift tubes are mounted. It has the first five drift tubes of the actual design, and the total length is approximately 0.5 m. The resonant frequency and unloaded quality factor (Q_0) were measured and are consistent with the CST-MW Studio calculation at 0.1% and 11%, respectively. The on-axis electric field distribution was measured using the bead-pull method [55] and agreed with the CST-MW Studio calculation within 3% uncertainty. The emittance growth owing to the field error is estimated to be 3%, which is negligible. A high power coupler was fabricated and a high power test will soon be conducted. Based on the experience with the prototype, we completed a detailed design of the actual IH-DTL and will soon start production.

2.5. DAW-CCL

After the IH-DTL, the DAW-CCL accelerates the muons to 40 MeV.

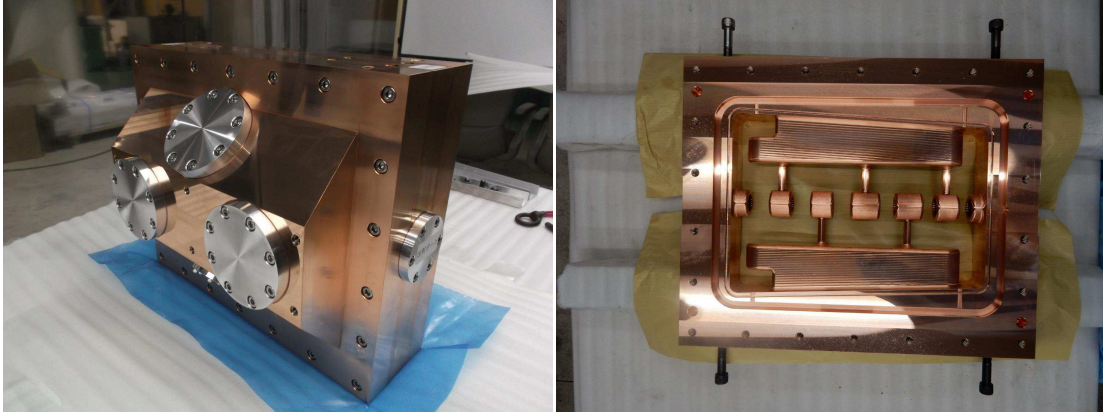


Fig. 9 Prototype of the IH-DTL: (Left) overall structure, (Right) center plate, where the five drift tubes are implemented.

A DAW-CCL is a cylindrical cavity with conductive washers placed across a disk-shaped disc. A DAW-CCL was first proposed in early 1970s [56, 57] and full scale cavity was demonstrated in late 1970s [58]. The first DAW-CCL was operated in a proton and H^- linac at the Moscow meson factory [59]. In Japan, DAW-CCLs were developed in KEK and Kyoto for electron [60, 61]. DAW-CCLs have advantages over other CCLs, such as a higher shunt impedance and higher coupling between the accelerating and coupling cells.

The DAW-CCL cavity is designed using several types of softwares [28]. As a first step, the two-dimensional dimensions are optimized using Poisson Superfish [62] for a higher acceleration efficiency and lower peak-to-average value (E_{\max}/E_0) in satisfying the confluence condition. After the two-dimensional calculation, the three dimensional calculations including the washer support are conducted using CST-MW Studio. The bi-periodic L-support [63], in which a washer is fixed by two supports and a pair of supports are located azimuthally 90 degrees apart from the adjacent supports, is adopted among several support structures because perturbation to the acceleration mode can be minimized by adjusting the support structure. Finally, the dispersion curve is investigated to check whether an unfavorable mode exists around the operation frequency.

Figure 10 shows the three-dimensional model (left) and the dispersion curve (right) of the designed cavity for $\beta = 0.3$. TM02 and TM01 are accelerating and coupling mode, respectively. Because of the bi-periodic structure, some stop bands appear in $\pi/2$. Although the TM11 mode is near the operational frequency, the cavity is tuned during the optimization process such that the operational frequencies sit within the stop band at $\pi/2$. Although the dipole mode passband TE11 crosses the line where the phase velocity matches the speed of the muons, it is not considered to be a problem because the muon beam current is negligible and the transverse kick owing to this mode is estimated to be much smaller than the requirement. Table 5 summarizes the cavity parameters for $\beta = 0.3, 0.4, 0.5$, and 0.6.

The beam dynamics is designed using PARMILA [64] and TRACE3D [65] based on the designed cavity performance. For ease of fabrication, a constant cell length ($L = \beta_s \lambda / 2$) in a tank with multiple cells is designed. The design velocity β_s and number of cells for each tank are determined based on the design of the beam dynamics. The inter-tank spacing is set to $4.5\beta\lambda$ considering the feasibility of a magnet installation. The average acceleration

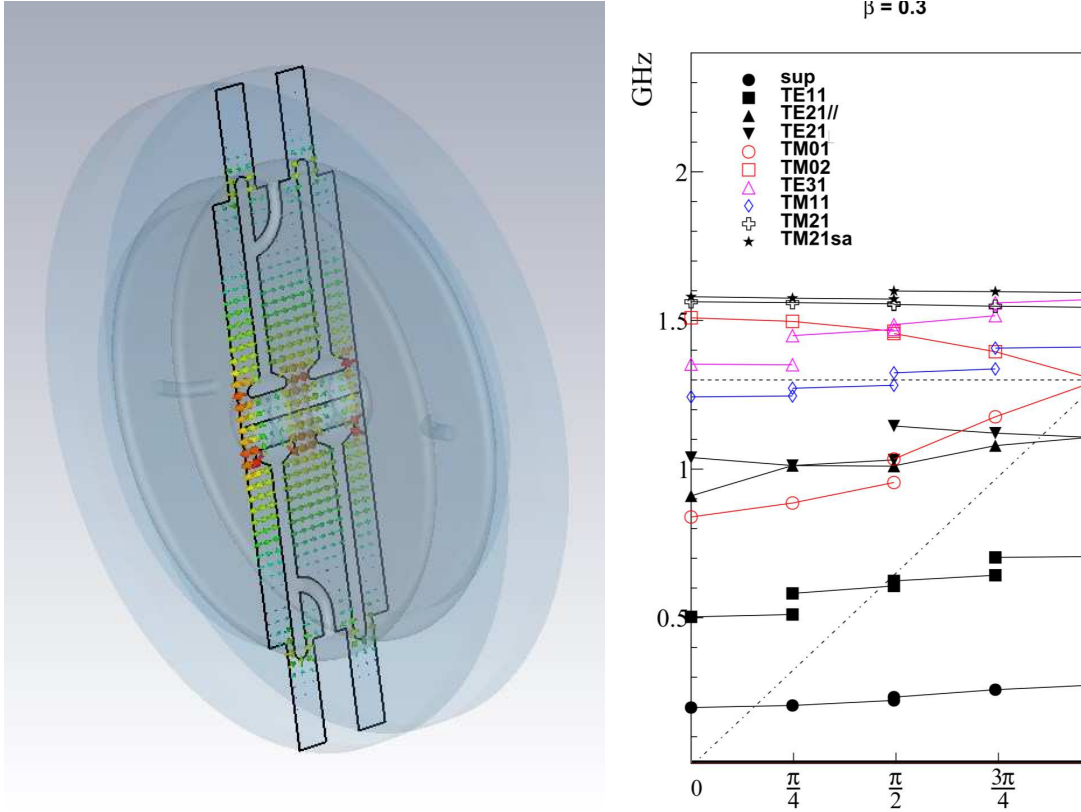


Fig. 10 (Left) Three-dimensional model of the DAW-CCL. The electric field of the acceleration mode in the two-cell model is shown by the colored arrows. (Right) Dispersion curve with optimized cavity in $\beta = 0.3$ calculated using CST-MW Studio. The dotted line represents target frequency (1.3 GHz) and the dashed line corresponds to the phase velocity of the muons. The sup mode is associated with the L-support.

field is determined to be 5.6 MV/m according to the Kilpatrick limit [66] and E_{\max}/E_0 ; the bravery factor is set to 0.9 in maximum. The number of cells in a tank is determined by the limitation of the quadrupole strength owing to transverse instabilities. There may be instabilities or resonances when the zero current phase advance (σ_0) is greater than 90 degrees [67]. Although the muon beam intensity is expected to be much smaller than that in the region of such instabilities, the number of cells is chosen to match this criterion. The maximum σ_0 is 83 degrees at the first tank when the number of cells is ten, which determines the number of cells for all tanks. Table 6 shows the basic parameters of each DAW tank. Because the shunt impedance of the DAW cell increases as a function of β , the power required for the tank decreases with a higher energy. The total power required is 4.5 MW. The *phase slippage* is the greatest in the first tank, ranging from -14 to $+10$ degrees.

The input distribution was given from the upstream IH-DTL simulation and used for the beam dynamics simulation after the calculation for the beam transport line to match the beam to the DAW-CCL. Figure 11 shows the phase space distributions at the DAW exit, and Table 7 summarizes the output beam parameters. The total length is 16.3 m with 15 modules, which corresponds to $138\beta\lambda$, and the beam transit time $t_{\text{trans.}}$ is calculated as

Table 5 Parameters of the DAW-CCL cavity for $\beta = 0.6, 0.5, 0.4,$ and 0.3 . For the simplicity, the resonant frequency is designed to be 1.3 GHz. In this Table, L is the cell length, f_a is the resonant frequency of the accelerating mode, f_c is the resonant frequency of the coupling mode, ZTT is the effective shunt impedance per unit length, E_{\max}/E_0 is the peak to average axial electric-field, and λ is the resonant wavelength.

Parameters	Values			
β	0.6	0.5	0.4	0.3
L	$\beta\lambda/4$			
f_a [GHz]	1.300	1.300	1.299	1.301
f_c [GHz]	1.299	1.301	1.302	1.301
ZTT[M Ω /m]	57.8	46.3	33.8	18.0
Transit time factor	0.84	0.85	0.84	0.81
E_{\max}/E_0	4.4	4.8	5.1	5.0
Q_0	2.91×10^4	2.41×10^4	1.91×10^4	1.42×10^4
Synchronous phase [deg.]	-30			

Table 6 Parameters of each DAW tank.

tank	N_{cells}	β_s	length [m]	Energy [MeV]	Power [MW]
1	10	0.29	0.34	5.6	0.39
2	↑	0.33	0.38	7.1	0.35
3	↑	0.37	0.42	8.8	0.33
4	↑	0.40	0.46	10.7	0.31
5	↑	0.43	0.50	12.7	0.30
6	↑	0.47	0.54	14.9	0.29
7	↑	0.50	0.57	17.2	0.29
8	↑	0.52	0.61	19.7	0.29
9	↑	0.55	0.64	22.3	0.28
10	↑	0.58	0.67	25.0	0.28
11	↑	0.60	0.69	27.9	0.28
12	↑	0.62	0.72	30.8	0.28
13	↑	0.64	0.74	33.8	0.28
14	↑	0.66	0.77	37.0	0.28
15	↑	0.68	0.79	40.2	0.28

$\frac{138\beta\lambda}{\beta c} = 106.0$ ns. The survival probability is calculated as $\exp(t_{\text{tran.}}/\tau_{\mu}\bar{\gamma}) = 96.1\%$, where $\bar{\gamma} = (\gamma_{\text{in}} + \gamma_{\text{out}})/2 = 1.212$. The emittance growth is estimated to be less than a few percent, and the output emittance is 0.32π and 0.21π mm mrad for the horizontal and vertical directions, respectively. The effect of errors on the emittance owing to a misalignment of the quadrupole magnet, power errors in the cavity, and other factors is evaluated to be less than 5% [68].

A cold model of the first DAW cells was fabricated to confirm the design. The cold model is made of aluminum. Figure 12 shows a mechanical drawing (left) and photograph of the

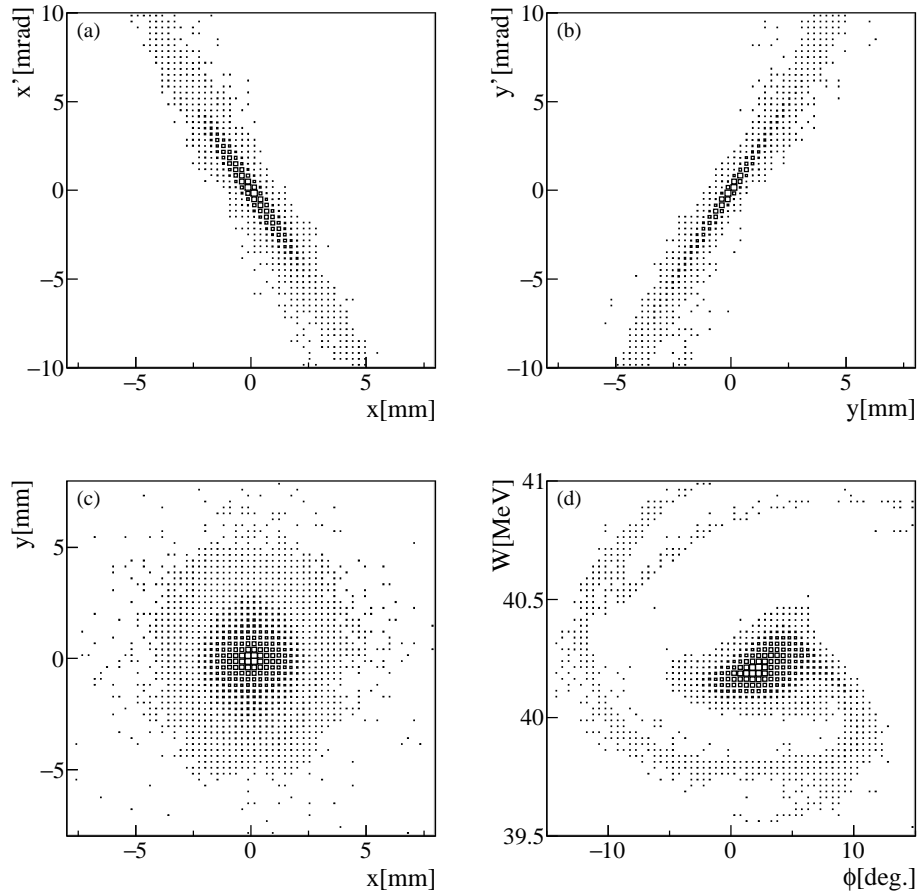


Fig. 11 Phase space distributions at the DAW-CCL exit: (a) Horizontal divergence angle x' vs. x , (b) vertical divergence angle y' vs. y , (c) y vs. x , and (d) ΔW vs. rf phase (= time)

assembly (right). The resonant frequency was measured and consistent with the calculation using CST-MW Studio at 0.4%. The on-axis electric field distribution was measured and the variation in the fields per cell was observed, which is considered to be due to the assembly process of the cavity. Based on the measurement results in the cold model, the actual DAW-CCL has been designed and the first tanks will be soon fabricated.

2.6. DLS

Finally, muons are accelerated to 212 MeV using the DLS.

DLS is classified as a radio-frequency linac for electron. After the first invention of the radio-frequency linac by Wideröe, Sloan and Lawrence [69, 70], Hansen studied an electromagnetic field with radio-frequency resonator for accelerating electron [71]. The acceleration of electron using a traveling wave accelerator was demonstrated in late 1940s [72]. Recent electron accelerators using room-temperature cavities have been based on the results of the Mark III linac [73] and SLAC. Unlike linear accelerators for electrons, which quickly reach the speed of light, muon linacs, which slowly approach the speed of light, require a gradual change in the length of the cell.

Table 7 Output beam parameters of the DAW-CCL. In this table, α and β are Twiss parameters.

	Output
α_x	4.1
β_x [mm/mrad]	0.23
ε_x [π mm mrad, rms, normalized]	0.332
α_y	-6.9
β_y [mm/mrad]	0.36
ε_y [π mm mrad, rms, normalized]	0.201
α_z	-0.002
β_z [deg/MeV]	24
ε_z [π MeV deg, rms, normalized]	0.108
Transmission	99.80%
Transient time	106 ns
Survival rate	96.1%
Transmission total	95.9%

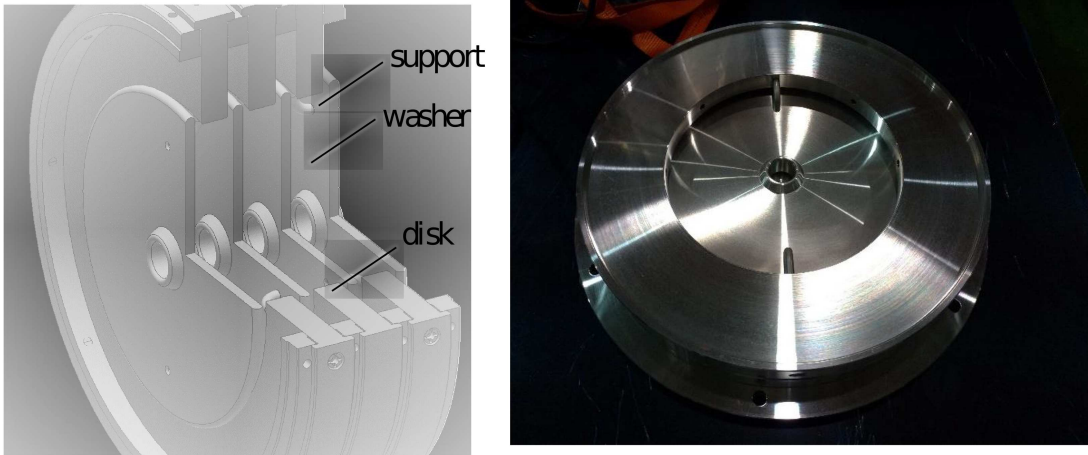


Fig. 12 Prototype of the DAW-CCL: (Left) mechanical three-dimensional drawing, (Right) assembly of the prototype. The end plate with the antenna ports is attached for the low power measurements.

The geometrical parameters of the DLS cell are designed using Poisson Superfish. Poisson Superfish generates the standing-wave-mode electric fields of each cell with open-open and short-short boundary conditions and the electric field of the traveling wave is represented by superposing these two fields with a phase difference of $\pi/2$. The L-band structure was adopted to make the acceptance sufficiently large for the input muon beam and the conventional $2\pi/3$ acceleration mode is adopted. The synchronous phase is set to -10 degrees to ensure sufficient longitudinal acceptance, and the average acceleration field (E_0) is assumed to be 20 MV/m. Figure 13 shows the parameters of the DLS cells. In this study, a constant

impedance desi,
beam dynamics
tributions at th
no emittance gr
the loss owing t

Fig. 13 Calculated cell parameters of the DLS section. D is the cell length calculated by $\beta\lambda/3$ and w is the kinetic energy of the muons.

Table 8 Output beam parameters of the DLS. In this table, α and β are Twiss parameters.

	Output
α_x	-1.9
β_x [mm/mrad]	0.86
ε_x [π mm mrad, rms, normalized]	0.331
α_y	-3.3
β_y [mm/mrad]	1.5
ε_y [π mm mrad, rms, normalized]	0.211
α_z	0.07
β_z [deg/MeV]	150
ε_z [π MeV deg, rms, normalized]	1.94
Transmission	99.9%
Transient time	30 ns
Survival rate	99%
Transmission total	99%

2.7. Summary of the muon linac design

Figure 15 shows the emittance evolution in the entire muon linac. There is no significant growth of the beam emittance and the output emittance is comparable to the required

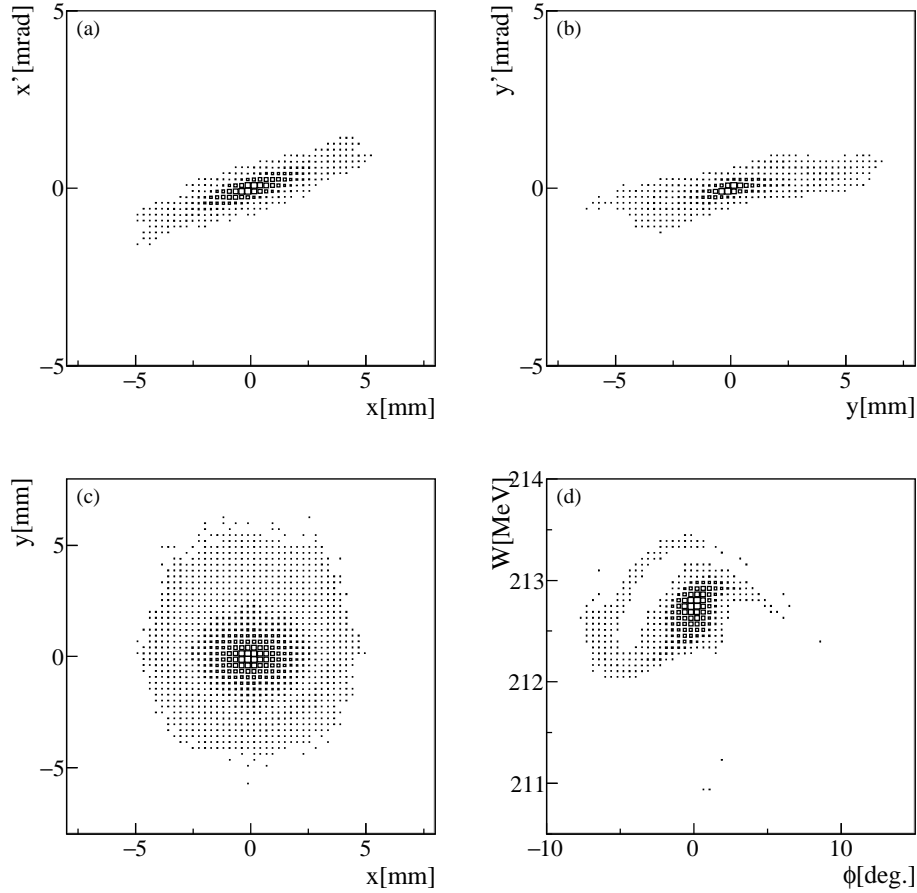


Fig. 14 Phase space distributions at the DLS exit: (a) Horizontal divergence angle x' vs. x , (b) vertical divergence angle y' vs. y , (c) y vs. x , and (d) ΔW vs. rf phase (= time)

total emittance of 1.5π mm mrad. Table 9 summarizes the transmission, decay loss, and emittance at each section. The intensity of the low emittance muon beam at the linac exit is estimated to be 1.2×10^4 muons per pulse with a repetition of 25-Hz. Table 10 shows the breakdown of the estimated transmission efficiency for all the experimental components and the statistical uncertainty of the a_μ measurement is estimated to be 450 ppb for 2.2×10^7 s of data taking [7]. The statistical precision is comparable to that of the BNL experiment, and we are able to examine the a_μ anomaly with a completely different scheme.

Table 9 Summary of the particle simulations through the muon linac: Transmission and decay loss in each section, and the emittance at the exit of each section. The transmission in SOA includes that of the mesh electrodes.

	Soa	RFQ	IH-DTL	DAW-CCL	DLS
Transmission [%]	56	95	100	100	100
Decay loss [%]	17	19	1	4	1
ε_x [π mm mrad, rms, normalized]	0.38	0.30	0.32	0.32	0.33
ε_y [π mm mrad, rms, normalized]	0.11	0.17	0.20	0.21	0.21

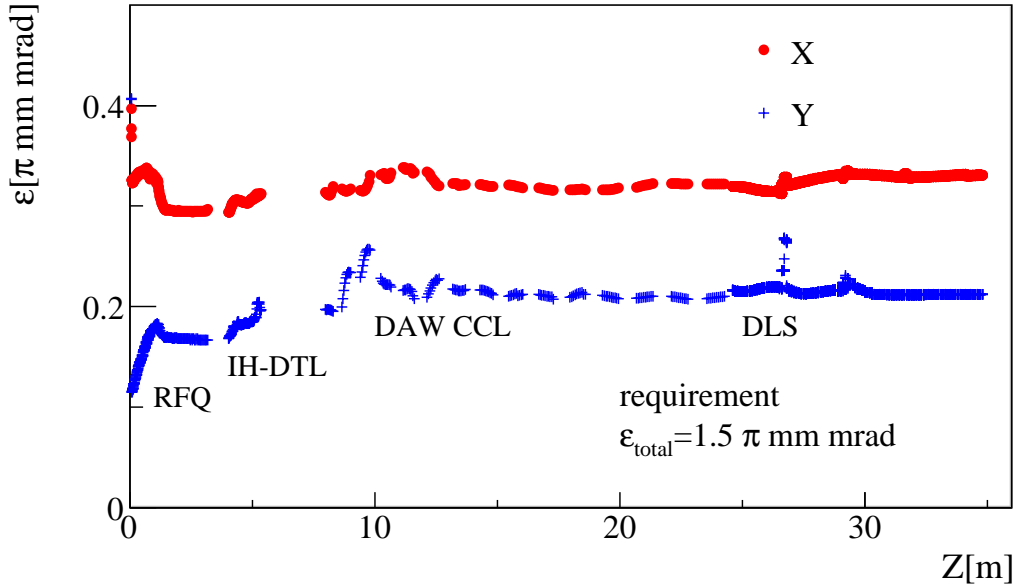


Fig. 15 Emittance evolution from the RFQ entrance to the linac exit.

Table 10 Breakdown of the estimated transmission efficiency. For the a_μ measurement, e^+ energy window (12%), detector acceptance (100%), and reconstruction efficiency (12%) should be considered. Details are described in [7].

	H-line	muonium emission	laser ionization	acceleration	injection	kicker
Transmission [%]	16	0.34	73	40	84	93

Because the systematic uncertainty is estimated to be less than 70 ppb and the measurement is statistically limited, further improvement of the beam intensity directly impacts the sensitivity of the physics. The goal in the next phase in the J-PARC E34 experiment is to measure a_μ with an accuracy of 100 ppb, comparable to the goal of the FNAL experiment. As shown in Table 10, primary improvement should be in the muonium emission efficiency. The next one is the H-line and the acceleration efficiency. According to the results of previous muonium measurements [17–19], the arrangement of the silica aerogel target is being investigated to enhance the overlap between the effective area of the target and the laser ionization region. In the muon linac, the most effective way for the improvement is a reduction of the decay loss in the low- β section. For this purpose, several efforts have been devoted: a new RFQ dedicated to the muons [26], an L-band RFQ combined with CC-DTL [74, 75], and a new scheme of acceleration for the low-energy muons [76].

Further, development is carried out for spin tracking [77]. Because a spin precession in the muon storage ring starts with the initial spin state determined by the muon linac exit, the initial state should be understood to examine the potential systematic uncertainties of the physics measurement. For this purpose, a spin tracking simulation is being developed. In

addition, a spin-rotator based on the Wien-filter type is designed to enable a spin-flipping analysis [78], which is usually used in many types of spin experiments.

3. Demonstration of muon acceleration

As described in Section 2, a low emittance muon beam is realized through thermal muon production and acceleration using the linac dedicated to the muons. The production of thermal muons has been developed for over a quarter of a century [79–81] and has matured sufficiently and can be used in experiments. Muon acceleration, however, was an unproven technology. Therefore, a muon acceleration should have been demonstrated prior to the construction of the actual linac. In addition, beam monitors are needed to diagnose the muon beam with an unprecedented beam size.

To demonstrate muon acceleration prior to the construction of the experimental setup that included the thermal muon source system, a faster and simpler system for slow muons was needed. The scheme of muon cooling using a simple metal degrader and acceleration using an RFQ proposed at Los Alamos National Laboratory [82] are suitable for this purpose. We basically followed this method, but to further reduce the emittance and separate accelerated muons from background high energy muons that pass through the RFQ without being accelerated, we decided to use negative muonium ions ($\mu^+e^-e^-$; Mu^-) produced through an electron capture process [83]. Prior to the demonstration of muon acceleration by Mu^- , an experiment dedicated to a Mu^- measurement was carried out to evaluate the expected amount of accelerating Mu^- signal.

This chapter describes the Mu^- measurement followed by a demonstration of muon acceleration along with a description of the development of the beam monitor.

3.1. Development of Mu^- source

As mentioned above, the Mu^- production process can be used to cool a muon beam down to 1 keV by simply irradiating positive muons (μ^+ 's) onto a thin metal film such as aluminum. However, since the first observation during the 1980s [83, 84], there have been no measurements or no proof that a significant intensity can be obtained for an acceleration test. Therefore, we decided to conduct the Mu^- measurement prior to the muon acceleration test.

In addition to the estimation of the accelerated muon signal, the method for identifying the background caused by positrons from muon decay (decay-positron) was also important. This is because the conversion efficiency from the primary μ^+ to Mu^- is expected to be less than 10^{-4} , which results in a large amount of decay-positrons derived from muon decays at the target. Therefore, the decay-positron background and low energy muon (LE- μ) measurements were carried out [85] using a micro-channel plate (MCP) detector (Hamamatsu photonics, F1217-01 [86]) in advance of the Mu^- measurements. In the decay-positron measurement, the decay-positrons from a muon beam target were identified by a series of triple scintillation detectors installed in front of the MCP detector. In the LE- μ measurement, the 7-keV μ^+ s are measured using the same setup as the Mu^- measurement described below. Figure 16 shows the pulse height distribution of the decay-positron (red triangle) and LE- μ (blue box). The difference between the decay-positrons and LE- μ in the pulse height distributions was evident, which can be explained by the single- and multi-channel amplification model described in Section 4 of [85]. The results show that event selection using the pulse

height can reject the decay-positron more than 75% while maintaining the muon efficiency at 90%.

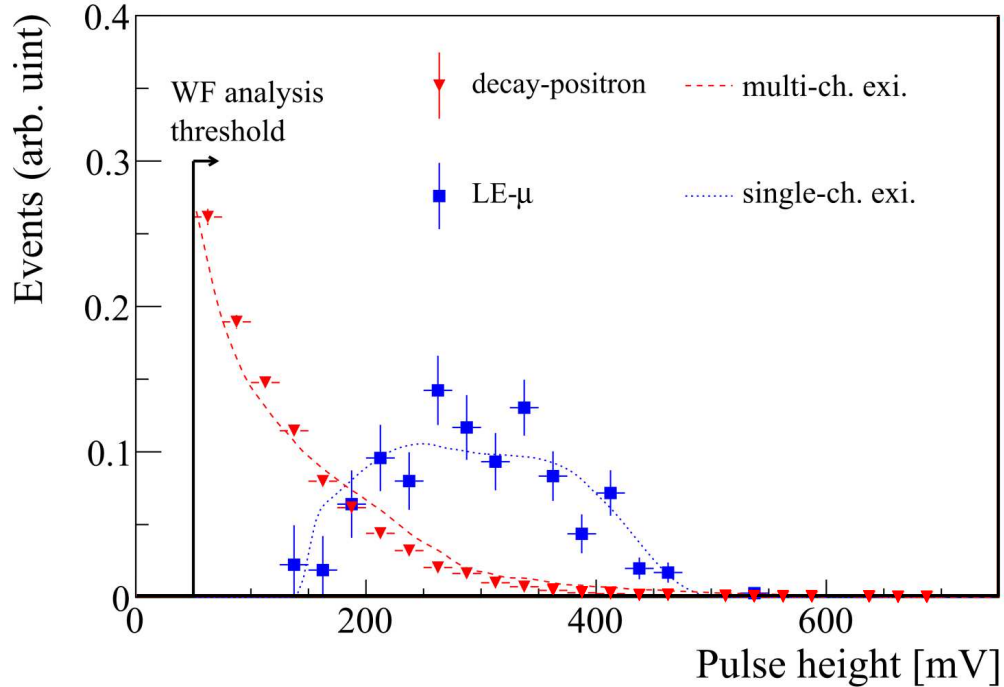


Fig. 16 Pulse height distribution for decay-positrons (red triangle) and $LE-\mu$ (blue box). Red dashed line and blue dotted line show the pulse height distribution with multi- and single-channel excitation models, respectively, as discussed in [85]. This figure is cited from [85].

The Mu^- measurements were conducted in a series of three experiments at the J-PARC MLF (2015A0324 [85], 2016A0067 [87], and 2018B0007 [88]). Figure 17 shows a typical setup for the experiments. The μ^+ 's were injected into a Mu^- production target after passing through a steel window. The Mu^- generated in the target was accelerated at up to 20 keV by the SOA electrostatic lens. Then, the Mu^- was transported to the detector location through a series of electrostatic quadrupole (EQ1-4), an electrostatic deflector (ED), and a bending magnet (BM). The energy acceptance of the beamline is estimated to be 1.4% by the GEANT4 simulation. The MCP detector was employed to measure the time of flight (TOF) from the Mu^- production target. The electrical signal from the MCP detector was amplified using a fast-filter amplifier (ORTEC 579) and digitized using CAEN V1720. The waveform within an interval of 10 μ sec around each 25-Hz beam pulse was recorded for analysis. A pulse higher than the noise level was regraded as a signal pulse. The leading edge of the signal pulse was defined as the signal timing. The pulse height is defined by the maximum height within the signal window of 40 ns. The μ^+ arrival time at the Mu^- production target was measured with a set of scintillating counters located at the side of the Mu^- production target.

In the 2015A0324 experiment, the $LE-\mu$ measurement was conducted to commission the experimental setup and compare the MCP signal to the decay-positron signal as described

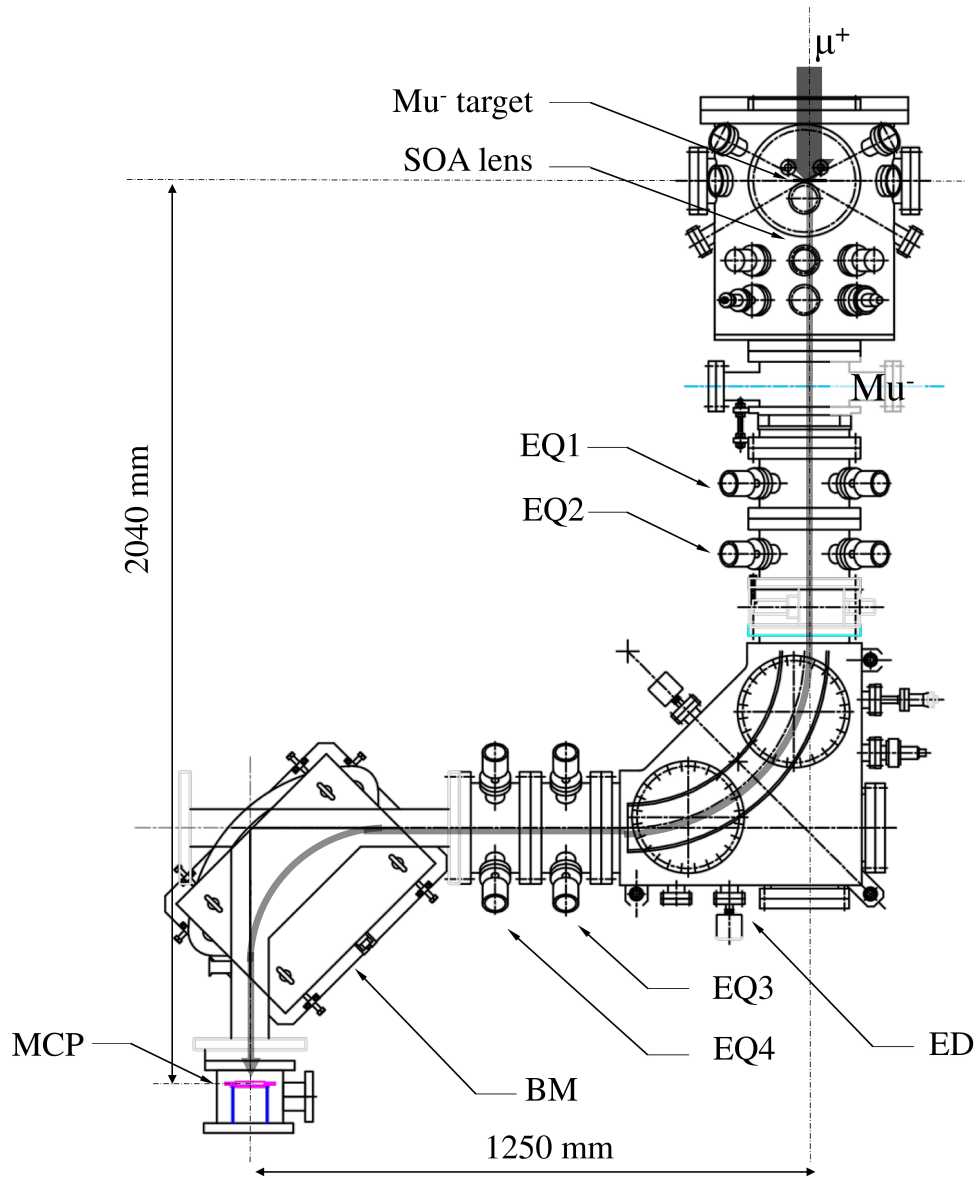


Fig. 17 Schematic of the typical experimental setup for the Mu^- measurements. This figure is cited from [88].

above. The aluminum (Al) thin foil is adopted as the target and $\text{LE-}\mu$ is extracted instead of Mu^- by flipping the beamline polarity and transported to the MCP detector. The $\text{LE-}\mu$ signal was used to tune the applied voltage of the quadrupole and other experimental setups. In addition to the tuning using the $\text{LE-}\mu$, negative hydrogen ions generated by ultraviolet light [89] were used for offline commissioning of the experimental setup.

The Mu^- s were observed during the 2016A0067 experiment, and high-statistics Mu^- data were obtained in the 2018B0007 experiment using three types of production targets: an Al foil, a C12A7 electride foil [90, 91], and a steel foil. The electrical signals of the MCP detector were recorded and analyzed in a way similar to the 2015A0324 experiment. Figure 18 (A) shows a pulse height versus the TOF of the observed signal. The background events are considered to be decay-positrons from muons stopped in the experimental apparatus, based

on the results of the analysis of time constants. The decay-positron events can be eliminated efficiently by the pulse height selection, as described above. After pulse height selection, the TOF distribution is obtained as shown in Fig. 18 (B). The two peaks at approximately -300 ns and 300 ns are due to prompt positrons carried through the surface muon beamline with the same momentum as μ^+ 's. Because the prompt positron is faster than μ^+ , the prompt positron arrives earlier than μ^+ . The blue and red curves show the fitting results assuming the remaining decay-positron background (blue) and the Mu^- signals (red), respectively. The background is consistent with the exponential decay curve with the muon decay constant ($\tau_\mu = 2.2 \mu\text{sec}$). The Mu^- peak width is consistent with that of the primary μ^+ beam. The time interval of the Mu^- peaks is consistent with that of the primary proton beam pulses. The Mu^- TOF is consistent within a few percentage points with the expectation estimated through the GEANT4 simulation where the initial energy of Mu^- is assumed to be 0.2 keV.

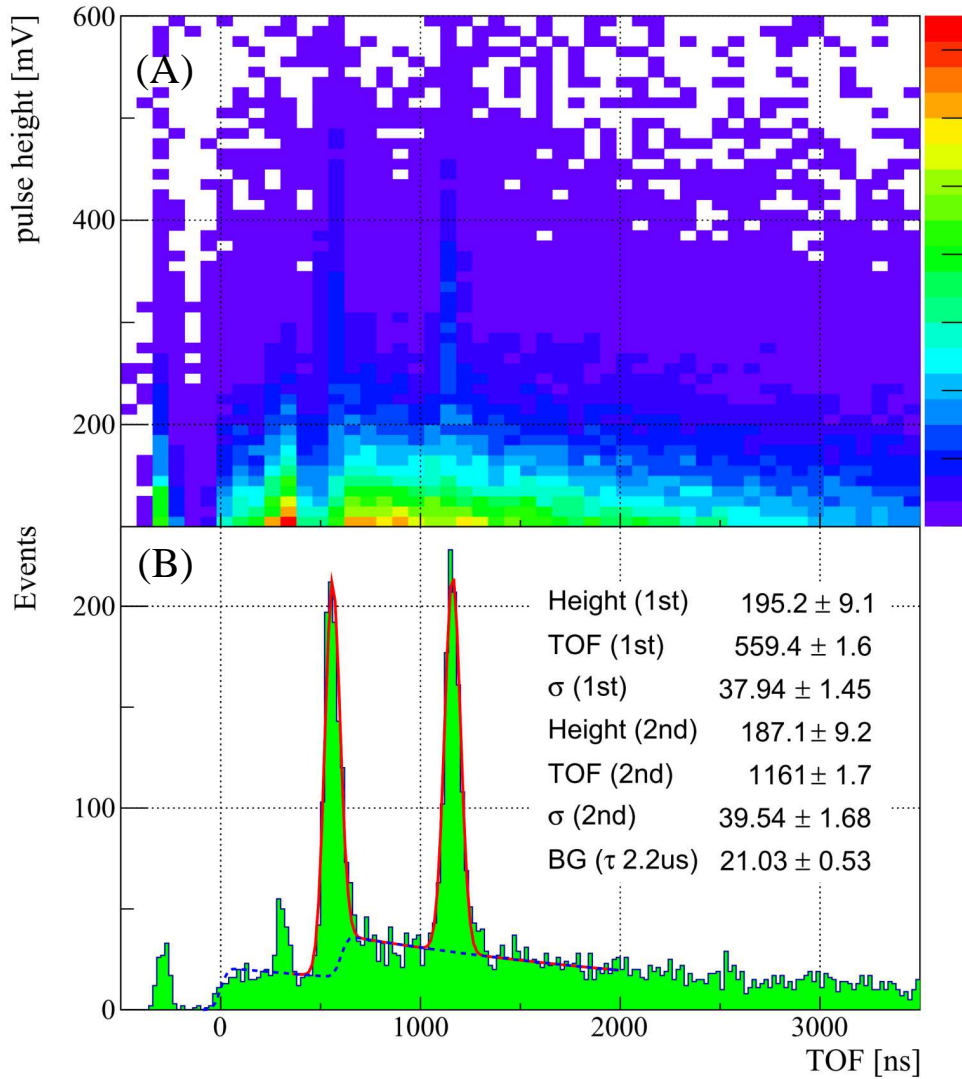


Fig. 18 (A) Pulse height vs. TOF for observed signal. (B) TOF distribution after pulse height selection. The solid red line and blue hatched line shows the fitting results assuming the Mu^- event and the decay-positron background. This figure is cited from [88].

Based on the measured Mu^- intensity during the 2016A0067 experiment, The expected intensity of the accelerated Mu^- signal was estimated to be 6.8 ± 1.2 (stat.) $_{-0.0}^{+0.4}$ (syst.)/s [87], where (stat.) represents the statistical error assigned by the measured Mu^- intensity in the experiment and (syst.) represents the systematic error. The effect of a misalignment of the Mu^- transport beamline is taken into account as a systematic error. From these results, it can be concluded that several hundred events of accelerated Mu^- signals can be expected with a beam time of a few days, and that the background of the decay-positrons can be sufficiently suppressed by a pulse height discrimination, such that a sufficient amount of the accelerated Mu^- 's can be observed with a sufficient signal-to-noise ratio.

3.2. First muon acceleration

A demonstration of the muon acceleration was conducted in J-PARC MLF over a 6-day period starting on October 24, 2017 (2017A0263) [1].

Figure 19 shows a schematic drawing of the experimental setup. The μ^+ 's were incident on the Al foil target used in the Mu^- measurements. The μ^+ 's were decelerated through the target, and some of the μ^+ 's become Mu^- 's at the downstream surface of the Al target. Using the same Soa lens as used in the Mu^- measurements, the generated Mu^- 's were accelerated to 5.6 keV and focused on the entrance of the RFQ. In this experiment, the prototype RFQ [92] was used. The length of this RFQ is equivalent to two-thirds of the RFQ in the muon linac, and this RFQ was originally designed using KEKRFQ [93] to accelerate negative hydrogen ions at up to 810 keV. To use this RFQ for a muon acceleration, the intervane voltage should be normalized to the muon mass, and the input velocity β should be the same as that of H^- . Table 11 summarizes the parameters of the prototype RFQ. The Mu^- 's are accelerated to 89 keV and then transported to the MCP detector through the diagnostic beamline consisting of two quadrupole magnets (QM1 and QM2) and a bending magnet (BM). Because the expected number of Mu^- signals is only a few hundred, and it is impossible to obtain the correct field setting using the Mu^- signals themselves, the diagnostic beamline was commissioned using negative hydrogen ions generated by ultraviolet light [89], and the field setting of the magnets was verified prior to the experiment. The electrical signals of the MCP detector are recorded in a similar way as the experiments of the Mu^- measurements.

Table 11 Parameters of the prototype RFQ for the H^- and muon acceleration.

	H^-	muon
Frequency (MHz)	324	
Number of cells	297	
Length (m)	1.97	
Intervane voltage (kV)	81	9.1
Power (kW)	180	2.3
Injection energy (keV)	50	5.6
Extraction energy (keV)	810	89

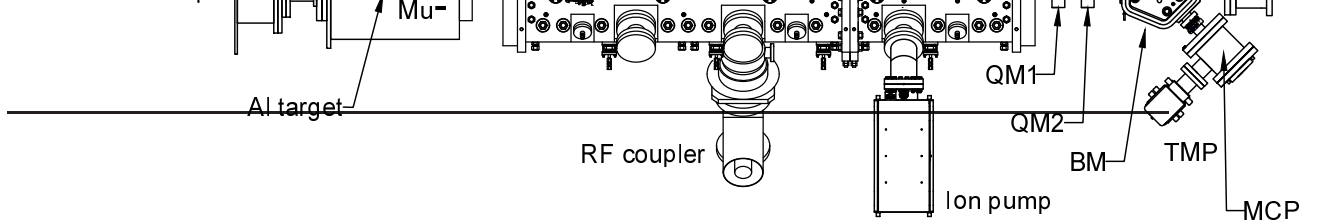


Fig. 19 Schematic drawing of the experimental setup for the demonstration of muon acceleration. In this figure, TMP is turbo molecular pump.

At the start of the experiment, the polarity of the beamline was set to transport positively charged particles. In this positive-charge configuration, muons that passed through the target and were decelerated to 89 keV, which corresponds to the acceleration energy, were measured. The observed TOF is consistent with calculations based on the distance between the target and the MCP detector and the velocity of the 89-keV muon. This confirms the beam diagnostic system.

After measurement of 89-keV μ^+ 's, the polarities of the magnets were flipped to a negative-charge configuration. Figure 20 shows the TOF spectrum with and without the RFQ operation after the pulse-height cut was applied. With the RFQ operation, a clear peak was observed at 830 ± 11 ns. The time required to reach the RFQ entrance from the target while being accelerated by the Soa lens was estimated as 307 ns using the GEANT4 simulation. The number of cells of the prototype RFQ is 297, and thus it takes $\frac{297}{2 \times 324 \times 10^6} = 458$ ns to fully accelerate the particles through the 324 MHz field. The length of the diagnostic beamline is 0.91 m, and thus the transit time of the 89-keV Mu^- is 72 ns. The total flight time of the accelerated Mu^- from the target to the MCP detector was calculated as $307 + 458 + 72 = 837$ ns, which is consistent with the measurement. The hatched histogram in Fig. 20 represents the simulated TOF spectrum of the accelerated Mu^- . The number of simulation events was normalized to the number of incident muons of this data set. The 46 ns rms width of the TOF spectrum is consistent with that from the timing distribution of the primary μ^+ at the Al target.

From these experimental results, it is concluded that the observed TOF peak is due to the Mu^- 's accelerated by the RFQ to 89 keV. The event rate was estimated as $(5 \pm 1) \times 10^{-4}/\text{s}$ by subtracting the decay-positron events estimated from the timing region outside the signal range. This is consistent with the expectation based on the Mu^- measurements. The intensity of the accelerated Mu^- is limited by the low conversion efficiency of μ^+ to Mu^- .

3.3. Development of beam monitors

After the first demonstration of the muon acceleration described above, the beam monitors for the accelerated muons were tested using the accelerated Mu^- 's. To diagnose the beam in

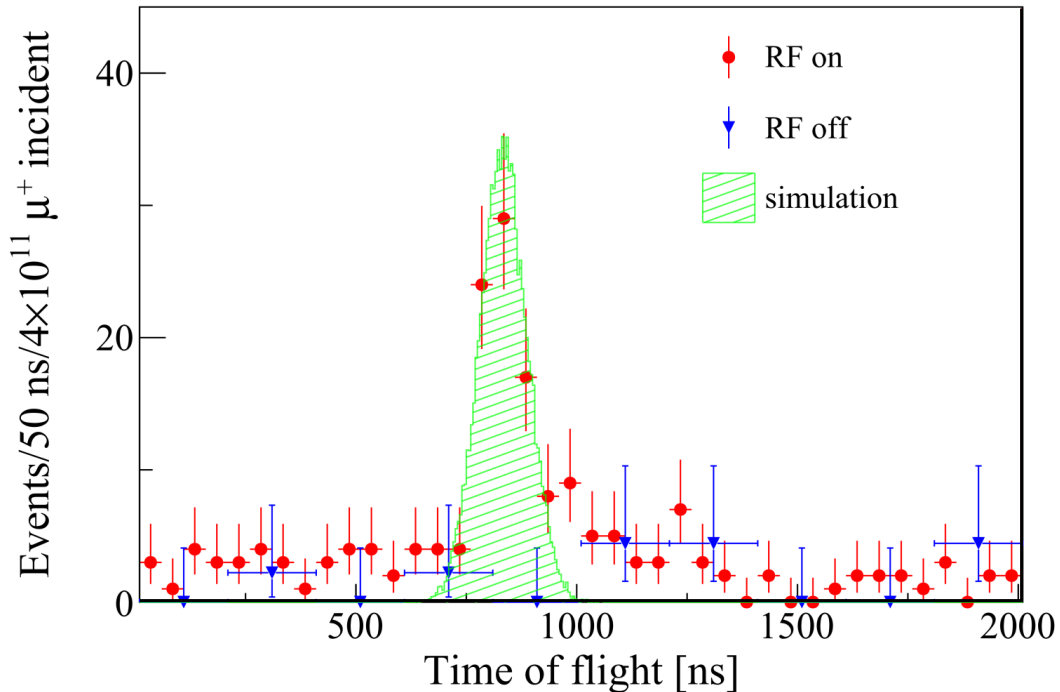


Fig. 20 TOF spectra of the negative-charge configuration with RF on and off. The clear peak of the RF on the spectrum at 830 ns corresponds to the accelerated Mu^- 's. The error bars are statistical. A simulated TOF spectrum of the accelerated Mu^- 's is also plotted. This figure is cited from [1].

both the transverse and longitudinal directions, a beam profile monitor (BPM) and a bunch width monitor (BWM) are necessary.

The BPM has been developed based on a MCP assembly (Hamamatsu F2225-21P) and a charge-coupled device (CCD) camera. The avalanche electrons generated by the MCP are injected into the phosphor screen, from which the light output is focused onto the CCD camera. The spatial resolution was estimated as 0.3 mm using an ultraviolet light and surface muons [94]. During the 2016B0214 experiment, the detector in the setup for the Mu^- measurement shown in Fig. 17 was replaced with the BPM and the performance against $\text{LE-}\mu$ was demonstrated [95]. During the 2017B0006 experiment, the detector in the setup shown in Fig. 19 is replaced with the BPM and the beam profiles of the accelerated Mu^- 's were measured. The Kolmogorov–Smirnov test was performed and the measurement and expectation were consistent within a statistical error (P-value is 21% and 38% for the horizontal and vertical direction, respectively) [96].

The BWM employed a MCP assembly (Hamamatsu F1217-11G) containing two stages of chevron-type MCPs. The signal-processing electronics of constant-fraction discriminators [97], which were adopted from the technology of the other experiment [98], measured the timing of the MCP signal. It detects single muon with a high temporal resolution, accumulates muon events, and reconstructs the beam bunch by taking the difference from the RF reference time of the muon linac. A test bench was developed to evaluate the temporal resolution of the BWM using a picosecond pulse laser (Hamamatsu PLP10-040) [99]. Recent results have evaluated the resolution of the BWM to be 40 ps, which corresponds to 1% of

the acceleration frequency of 324 MHz and satisfies the requirement. During the 2018A0222 experiment, the detector in the setup shown in Fig. 19 is replaced with the BWM to measure the bunch width of the accelerated Mu^- 's. In addition, a buncher cavity developed as a prototype for the muon linac [100] was installed between QM2 and BM to focus the beam in the longitudinal direction. The bunch width was successfully measured to be 0.54 ± 0.11 ns, which is consistent with the simulation [101].

From these measurements, the beam monitors are ready to diagnose the accelerated muon beam, particular for low energy part. Because these monitors are based on an MCP and the detection efficiency of an MCP is expected to decrease as the muon energy increases, to conduct sufficient beam commissioning, it is necessary to develop a beam monitor for the high-energy part.

4. Summary and outlook

The design of the muon linac for the J-PARC E34 experiment and the first muon acceleration were presented. The experiment for demonstrating the acceleration of the thermal muons is scheduled in 2022 at a new muon experiment area (S2) in J-PARC MLF. The experiment aims to study the laser ionization of the muonium via the 1S-2S excitation with 244-nm laser [102] and to accelerate the thermal muons using the RFQ. The muon beam emittance before and after the acceleration will be measured using the beam monitors described in Section 3.3. After the experiment at S2, the muon acceleration using the RFQ and IH-DTL at the H-line will be conducted.

We are entering a new era in which the accelerated muons are available. One can naturally imagine an imaging technique with accelerated muons, allowing for a better resolution with less time than cosmic-ray muons. It is natural to think of a collider using an accelerated muon beam. A type of collider in which muons collide with other particles has been actively discussed [103, 104]. If a cooling method of negative muons with an efficiency comparable to that of the muonium laser ionization is realized, a muon collider will be promised.

The J-PARC E34 experiment will soon be realized as a flagship to new horizon for a better understanding of nature.

Acknowledgment

We express our appreciation to the many manufacturing companies involved in this project, especially to Toshiba Co., who fabricated the prototype RFQ, Toyama Co.,Ltd., who fabricated the actual RFQ, and TIME Co., Ltd., who fabricated the buncher cavity and the prototype IH-DTL. This work is supported by JSPS KAKENHI (Grant Numbers , 25800164, 15H03666, 15H05742, 16H03987, 16J07784, 18H03707, 18J22129, 19J21763, 20J21440, 20H05625, 21K18630, 21H05088, 22H00141) , JST FOREST Program (Grant Number JPMJFR2120) and the natural science grant of the Mitsubishi Foundation. This work is also supported by the Korean National Research Foundation grants NRF-2015H1A2A1030275, NRF-2015K2A2A4000092, and NRF-2017R1A2B3007018; the Russian Foundation for Basic Research grant RFBR 17-52-50064; and the Russian Science Foundation grant RNF 17-12-01036. This experiment at the Materials and Life Science Experimental Facility of the J-PARC was performed under user programs (Proposal No. 2015A0324, 2016A0067, 2016B0214, 2017A0263, 2017B0006, 2018A0222, and 2018B0007).

References

- [1] S. Bae et al., Phys. Rev. AB 21, 050101 (2018).
- [2] S.H. Neddermeyer, C.D. Anderson, Phys. Rev. 51, 884 (1937).
- [3] E. G. Michaelis, IEEE Trans. Nucl. Sci. Vol. NS-23, No. 3, 1385 (1975).
- [4] M. Boscolo, J. P. Delahaye and M. Palmer, Rev. Acc. Sci. Tech., Vol 10, No. 01, 189-214 (2019)
- [5] M. Boscolo et al., Phys. Rev. AB 21, 061005 (2018).
- [6] https://slowmuon.kek.jp/index_e.html
- [7] M. Abe et al., Prog. Theor. Exp. Phys. 2019, 053C02 (2019).
- [8] G. Charpak, F. J. M. Farley, R. L. Garwin, T. Muller, J. C. Sens, and A. Zichichi, Phys. Lett. 1, 16 (1962).
- [9] J. Bailey et al., Nuovo Cimento A 9, 369 (1972).
- [10] J. Bailey et al., Nucl. Phys. B 150, 1 (1979).
- [11] Bennett G. W. et al. (Muon $g - 2$ Collaboration), Phys. Rev. D 73, 072003 (2006).
- [12] T. Aoyama et al., Phys. Rept. 887, 1 (2020).
- [13] J. Grange et al. (Muon $g - 2$ Collaboration), arXiv:physics.ins-det/1501.06858
- [14] B. Abi et al. (Muon $g - 2$ Collaboration), Phys. Rev. Lett. 126, 141801 (2021).
- [15] D. Stratakis et al., Phys. Rev. AB 22, 011001 (2019).
- [16] N. Kawamura et al., Prog. Theor. Exp. Phys. 2018, 113G01 (2018).
- [17] Bakule P. et al., Prog. Theor. Exp. Phys. 2013, 103C01 (2013).
- [18] G.A. Beer et al., Prog. Theor. Exp. Phys. 2014, 091C01 (2014).
- [19] J Beare et al., Prog. Theor. Exp. Phys. 2020, 123C01 (2020).
- [20] H. Inuma et al., Nucl. Instrum. Meth. A 832, 51 (2016).
- [21] M. Abe et al., Nucl. Instrum. Meth. A 890, 51 (2018).
- [22] T. Aoyagi et al., JINST 15, P04027 (2020).
- [23] T. Kishishita et al., IEEE TNS, 67, 2089 (2020)
- [24] Y. Kondo et al., Phys. Rev. AB 16, 040102 (2013).
- [25] M. Kubosaki et al., Proceedings of PASJ 2011, 1366 (2011).
- [26] Y. Kondo et al., Proceedings of IPAC 2015, 3801 (2015).
- [27] M. Otani et al., Phys. Rev. AB 19, 040101 (2016).
- [28] M. Otani et al., J. Phys. :Conf. Ser. 1350, 012097 (2019).
- [29] Y. Kondo et al., J. Phys. :Conf. Ser. 875, 012054 (2017).
- [30] K. F. Canter, P. H. Lippel, W. S. Crane, and A. P. Mills Jr., in "Positron studies of solids, surfaces and atoms" (World Scientific, Singapore, 1986) p. 199.
- [31] M. Otani et al., J. Phys. :Conf. Ser. 1067, 052018 (2018).
- [32] G4beamline, <http://public.muonsinc.com/Projects/G4beamline.aspx>
- [33] P. Strasser et al., Journal of Physics: Conference Series 225, 012050 (2010).
- [34] GEANT4, <http://geant4.cern.ch/>
- [35] OPERA3D, Vector Fields Limited, Oxford, England., <https://operafea.com/>
- [36] K. R. Crandall et al., LA-UR-96-1836 (2005).
- [37] I.M. Kapchinskiy and V.A. Tepliakov, Prib. Tekh. Eksp 2, 19-22 (1970).
- [38] I.M. Kapchinskiy and V.A. Tepliakov, Prib. Tekh. Eksp 4, 17-19 (1970).
- [39] J.E. Stovall, K.R. Crandall, R.W. Hamm, IEEE Trans. Nucl. Sci. NS-28 p.1508 (1981)
- [40] M. Otani et al., Proceedings of PASJ 2015, 56 (2015)
- [41] H. Morinaga, Phys. Soc. Meeting, Osaka (1949).
- [42] J.P. Blewett, Proceedings of Symposium du CERN sur les Accelérateurs de Haute Energie et la Physique des Mesons π v.1, 162 (1956).
- [43] P.M. Zeidlitz and V.A. Yamnitskii, J. Nucl. Energy, Part C4, 121 (1962).
- [44] J. Pottier, IEEE Trans. Nucl. Sci. 16/3, 377 (1969).
- [45] E. Nolte et al., Nucl. Instr. and Meth. 158, 311 (1979).
- [46] U. Ratzinger, CERN Yellow Report, 2005-003, 351 (2005).
- [47] Good, M.L., Phys. Rev. 92, 538 (1953).
- [48] S. Minaev and U. Ratzinger, Proceedings of PAC Conf 1999., 3555 (1999).
- [49] Y. Iwata et al., Nucl. Instr. Meth. A569, 685 (2006).
- [50] R. A. Jameson, arXiv:physics.acc-ph/1404.5176
- [51] CST Studio Suite, Computer Simulation Technology (CST). <https://www.cst.com/products/CSTMWS>
- [52] M. Otani et al., Proceedings of the PASJ 2016, 858-862 (2016).
- [53] General Particle Tracer, Pulsar Physics. <http://www.pulsar.nl/gpt/>
- [54] Y. Nakazawa et al., J. Phys. :Conf. Ser. 1350, 012054 (2019).
- [55] Peter A. McIntosh, Proceedings of 4th European Particle Accelerator Conference, 1283 (1994).

-
- [56] V. G. Andreev et al., Proceedings of Linear Accel. Conf 1972, 114 (1972)
- [57] B.P. Murin et al., Proceedings of Proton Linac Conf 1972, LA-5115, p.387 (1972).
- [58] V.G.Andreev et al., Proceedings of Linac Conf. 1976, AECL-5677 p.269 (1976).
- [59] S. K. Esin et al., Proceedings of Linear Accel. Conf 1988. 657 (1988)
- [60] S. Inagaki, Nucl. Instrm. and Meth. in Phys. Res. A 251, 417-436 (1986).
- [61] Y. Iwashita, Nucl. Instrm. and Meth. in Phys. Res. A 348, 15-33 (1994).
- [62] J.H. Billen and L.M. Young, Los Alamos Report, LA-UR-96-1834 (1996).
- [63] H. Ao et al., Jpn. J. Appl. Phys. 39, 651 (2000).
- [64] <http://www.laocg.lanl.gov>
- [65] K.R. Crandall and D.P Rustoi, Los Alamos Report, LA-UR-97-886 (1997).
- [66] W.D. Kilpatrick, Rev. Sci. Instr. 28, 824 (1957).
- [67] Reiser M "Theory and Design of Charged Particle Beams"1994 JOHN WILEY & SONS, INC.
- [68] Y. Takeuchi et al., to be published in proceedings of J-PARC symposium.
- [69] R. Wideröe, Arch. Electrotech., 21, 387 (1928).
- [70] D.H. Sloan and E.O. Lawrence, Phys. Rev. 38, 2021-2032 (1931).
- [71] H. Hansen, J. App. Phys. 9, 654 (1938)
- [72] E.L. Ginzton, W.W. Hansen and W.R. Kennedy, Rev. Sci. Instrum, 19, 89 (1948)
- [73] M. Chodorow et al., Rev. Sci. Instrum. 26, 134 (1955).
- [74] Y. Kondo, M. Otani, Proceedings of PASJ2020, 218 (2020) (in Japanese).
- [75] Y. Kondo, T. Morishita, J. Tamura, M. Otani, Proceedings of LINAC 2018, 794 (2018).
- [76] M. Otani, Y. Kondo, Proceedings of PASJ2020, 202 (2020) (in Japanese).
- [77] H. Yasuda et al., Proceedings of PASJ2020, 173 (2020) (in Japanese).
- [78] H. Yauda et al., to be published in proceedings of J-PARC symposium.
- [79] A. P. Mills, Jr., J. Imazato, S. Saitoh, A. Uedono, Y. Kawashima, and K. Nagamine Phys. Rev. Lett. 56, 1463 (1986).
- [80] Steven Chu, A. P. Mills, Jr., A. G. Yodh, K. Nagamine, Y. Miyake, and T. Kuga Phys. Rev. Lett. 60, 101 (1988).
- [81] K. Nagamine et al., Phys. Rev. Lett. 74, 4811 (1995)
- [82] H. Miyadera et al., in proceedings of PAC 2007, 3032 (2007).
- [83] Y. Kuang et al., Phys. Rev. A39, 6109 (1989)
- [84] D.R. Harshman, et al., Phys. Rev. Lett. 56, 2850 (1986).
- [85] M. Otani et al., Nucl. Inst. Meth. Phys. Res. Sec. 946, 162693 (2019).
- [86] <http://www.hamamatsu.com/>
- [87] R. Kitamura et al., to be published in Phys. Rev. AB.
- [88] M. Otani et al., J. Phys. :Conf. Ser. 1350, 012067 (2019).
- [89] Y. Nakazawa et al., Nucl. Inst. Meth. Phys. Res. Sec. 937, 164 (2019).
- [90] H. Hosono et al., Science, 301, 626 (2003).
- [91] H. Hosono et al., Proc. Natl. Acad. Sci. USA 114(2), 233 (2017).
- [92] Y. Kondo, K. Hasegawa, and A. Ueno, Proceedings of LINAC 2006, 749 (2006).
- [93] A. Ueno and Y. Yamazaki, Proceedings of Linac Conf. 1990, 329 (1990).
- [94] B. Kim et al., Nucl. Inst. Meth. Phys. Res. Sec. A. 899, 22 (2018).
- [95] R Kitamura et al., J. Phys. :Conf. Ser. 875, 012055 (2017).
- [96] M. Otani et al., J. Phys. :Conf. Ser. 1067, 052012 (2018).
- [97] B. Leskovar and C. C. Lo, Nucl. Instrum. Meth. Phys. Res., Sect. A123, 145 (1975).
- [98] K. Inami (Belle-II PID Group), Nucl. Instrum. Meth. Phys. Res., Sect. A766, 5 (2014).
- [99] M. Yotsuzuka et al., Proceedings of IPAC2019, 2571 (2019).
- [100] M. Otani et al., Nucl. Inst. Meth. Phys. Res. Sec. A 946, 162693 (2019).
- [101] Y. Sue, M. Yotsuzuka et al., Phys. Rev. Accel. Beams 23, 022804 (2020).
- [102] Ce Zhang et al., JPS Conf. Proc. 33, 011125 (2021).
- [103] M. Lu et al., arXiv:physics.hep-ph/2010.15114
- [104] K. Cheung, Z. S. Wang., arXiv:physics.hep-ph/2101.10476